Thin Solid Films 593 (2015) 71–80

Contents lists available at ScienceDirect

Thin Solid Films

journal homepage: www.elsevier.com/locate/tsf

Study of the mechanical behavior and corrosion resistance of hydroxyapatite sol–gel thin coatings on 316 L stainless steel pre-coated with titania film

Djahida Sidane [a,*], Didier Chicot [b], Sabeha Yala [a], Salima Ziani [a], Hafit Khireddine [a], Alain Iost [c], Xavier Decoopman [b]

[a] Laboratoire de Génie de l'Environnement, Département de Génie des Procédés, Université de Bejaia, Route Targa Ouzemour, Bejaia 06000, Algeria
[b] Laboratoire de Mécanique de Lille, LML, UMR 8107, UST Lille, IUT A GMP, BP 90179, 59 653 Villeneuve d'Ascq, France
[c] MSMP, Arts et Métiers ParisTech, 8, Boulevard Louis XIV, 59000 Lille Cedex, France

ARTICLE INFO

Article history:
Received 17 November 2014
Received in revised form 13 September 2015
Accepted 17 September 2015
Available online 25 September 2015

Keywords:
Hydroxyapatite
Titania
Sub-layer
Mechanical behavior
Corrosion test

ABSTRACT

In order to reinforce the clinical applications of hydroxyapatite (HAP) sol–gel coatings deposited onto 316 L stainless steel, we suggest the introduction of an intermediate thin layer of titania (TiO_2) on the substrate. The titania sub-layer is introduced in order to improve both the corrosion resistance and the mechanical properties of the HAP/316 L stainless steel coated system. The two coatings, HAP and TiO_2, were studied separately and afterwards, compared with the bi-layered coating. A film without any cracks is obtained under the optimum conditions in terms of annealing temperature, dipping rate and aging effect. Microstructural, morphological and profilometry analysis revealed the non-stoichiometric carbonated porous nature of the hydroxyapatite coatings, which were obtained after annealing at 500 °C during 60 min in the atmosphere. The obtained TiO_2 coatings exhibit a dense and uniform surface. Addition of TiO_2 as sub-layer of the HAP coating tends to increase the homogeneity and the crystallinity rate as compared to the HAP one.

The mechanical properties, i.e. hardness and elastic modulus, are determined by means of nanoindentation experiments and the adhesion between the coating and substrate is estimated by scratch tests. The corrosion behavior is evaluated by potentiodynamic cyclic voltammetry tests. As a main result, the values of the elastic modulus and hardness, respectively of 30 GPa and 2.5 GPa, are relatively high for the HAP–TiO_2 bilayer coating. This result allows the use of such coated material as a replacement material for hard tissues. The adhesion strength increased from 2925 mN up to 6430 mN after the addition of the TiO_2 intermediate film. According to the Tafel's analysis, the 316 L stainless steel specimens coated with both HAP and titania layers ($E_{Corr} = -234$ mV, $I_{Corr} = 0.089$ μA cm^{-2}) present a better resistance than the HAP-coated specimens ($E_{Corr} = -460$ mV, $I_{Corr} = 0.860$ μA cm^{-2}).

1. Introduction

Thin titania coatings on 316 L stainless steel have the combined advantages of biocompatibility and corrosion resistance [1,2]. Consequently, the use of Titania as a bonding oxide film between the hydroxyapatite and the substrate is studied with the objective of improving the global properties of the HAP coatings [3–7]. In this work, we propose a strategy of HAP coating with the introduction of TiO_2 oxide ceramic at the surface of the 316 L stainless steel substrate in order to improve the corrosion resistance, the mechanical properties and the bonding strength of the bilayer HAP–TiO_2 bioceramic coating. The coatings were obtained by the sol–gel dip coating process due to its simplicity, and also because it allows the preparation of high-quality thin films on metal substrates [8,9]. Moreover, it has been reported in the literature that the coated materials prepared by sol–gel deposition are more bioactive than those prepared by other methods [10,11]. The main objective of this study is to evaluate the mechanical behavior of sol–gel hydroxyapatite and hydroxyapatite–titania bilayer coatings on 316 L stainless steel.

In a previous work [12], we determined the hardness of the HAP single and the bi-layered coating systems by means of classical microindentation tests. The model of Jönsson and Hogmark was applied to separate the two contributions of the substrate and of the film in the measured hardness in order to determine the hardness of the film only.

* Corresponding author at: Université Abderrahmane Mira, Route Targa Ouzemour, Bejaia 06000, Algeria.
E-mail address: dj.sidane@yahoo.fr (D. Sidane).

http://dx.doi.org/10.1016/j.tsf.2015.09.037
0040-6090/

In this paper, additional studies have been performed using the continuous stiffness measurement mode in nanoindentation in order to determine the hardness of the film as a function of the indenter displacement. Consequently, nanoindentation provides a useful comparison with the mechanical properties of the surrounding coatings and underlying substrate. Various methods can be employed to address the problem of determining the hardness and elastic modulus of thin films when the substrate is involved in the deformation process occurring during the indentation experiments. Only few publications present in detail the determination of the elastic modulus and the hardness of thin hydroxyapatite sol–gel films (<2000 nm in thickness) directly and properly from the indentation data. The determination of the mechanical properties of relatively thin coatings by nanoindentation often requires the application of models for separating the contribution of the substrate from the indentation data [13,14]. For hardness measurements, a model must be applied when the indenter displacement is higher than a given value, which depends both on coating thickness and the mechanical behavior of the coating, i.e. for a hard coating on a soft substrate or for a soft coating on a hard substrate. For example, Bückle [15] and Sun. et al. [16] indicate a value for the indenter displacement close to 10% of the coating thickness after which the substrate interferes with the measurement. Unfortunately, this limit of 10% is not a predictable value. When considering the elastic modulus determination, this limit value can be much less. Indeed, this value is close to 1% of the film thickness for a hard film deposited onto a soft substrate [17,18] and it can reach 20% for a soft film deposited onto a hard substrate [19,20]. As a consequence, to avoid the application of models for which the above mentioned limit values cannot be defined precisely and also for which the accurateness significantly depends on the adjustment of the intrinsic fitting parameters to the model, a direct determination of the mechanical properties of the material will be preferable. This is rendered possible by means of the continuous stiffness measurement mode, which allows the computation of both the hardness and the elastic modulus as a function of the indenter displacement [21]. Moreover, under these conditions, the mechanical properties can be obtained for very low indenter displacements, typically less than 50–100 nm. According to the nature of these variations, application of models may or may not be required. In this work, we suggest the study of the mechanical properties by analyzing the variation of the hardness and the elastic modulus as a function of the indenter displacement.

Regarding the application of coated systems, the adhesion strength between the coating and its substrate is a very important parameter, which must be studied by means of scratch tests. These tests performed with a spherical diamond indenter, allow the determination of the critical load corresponding to the removal of the coating. This critical load can be used as an adhesion criterion.

There is always concern about the corrosion resistance of the 316 L stainless steel in physiological fluids. For this reason, the development of the biomedical implants requires the improvement of their corrosion resistance. In this paper, the influence of the bilayer hydroxyapatite–titania film on the corrosion resistance of the 316 L stainless steel in simulated human body fluids has been examined. The experiments were conducted using open circuit potential and potentiodynamic cyclic voltammetry tests.

2. Materials and experiments

Specific amounts of phosphorus pentoxide (P_2O_5, Prolabo 100%) and calcium nitrate tetrahydrate ($Ca(NO_3)_2.4H_2O$, Fluka 98%) were dissolved in absolute ethanol to form different solutions with concentrations of 0.5 mol/l and 1.67 mol/l, respectively. These two solutions were mixed to obtain the HAP sol having Ca/P molar ratio of 1.67 [22]. The mixture was continuously stirred at room temperature for 24 h. This produces a translucent sol. Titanium isopropoxide (TIP, Fluka 100%) was used as a titania precursor in the sol–gel process. The reactivity toward water is modified by acetic acid (HOAc) (molar ratio of TIP/HOAc = 1/10), which is also used as catalyst. 2-methoxy ethanol was added to adjust the degree of viscosity of the solution. This solution with titanium molar concentration of approximately 0.47 M was vigorously stirred at room temperature [23].

Finally, the resultant HAP sol was closely capped and aged for 24 h at room temperature. In the same way, TiO_2 sol was kept closely capped and aged for 24 h at the temperature of 100 °C. The effect of temperature of TiO_2 aging sol on the film morphology has been discussed and detailed in [12].

316 L stainless steel is used as the substrate. The dimensions of the samples are 20 × 10 × 5 mm. Before deposition, the samples were mechanically polished using different silicon carbide grit papers from 120 to 1200 grades. Mirror polishing was done using diamond paste of 2 μm and of 0.7 μm in the final step. The substrate samples were ultrasonically degreased with acetone and washed with running double distilled water. Finally, they were dried at 150 °C during 10 min. The TiO_2 coatings were obtained by dipping the polished, washed and dried substrates in the suspension at the dipping rate of 20 mm/min and annealed at 450 °C during 60 min. Dipping of the hydroxyapatite suspension was maintained in the range of 10–80 mm/min and annealed at different temperatures, i.e. 500 °C, 600 °C, 700 °C and 750 °C during 60 min in air. The HAP particles were deposited onto the surface of the TiO_2 film with the optimized parameters.

The different phases present in the coatings were identified by X-Ray diffraction (XRD) analysis, (panalytical type MPD/system vertical θ/θ), using radiation source (CuKα = .5406 Å) operating at 40 kV and 30 mA. The XRD diffraction patterns were collected over a 2θ range located between 20° and 80° using an incremental step size of 0.02° with 6 s of acquisition time per step. The identification of the phases was performed by comparing the experimental XRD patterns to standards compiled by the International Center for Diffraction Data (ICDD).

The microstructure analysis for identifying the different species and the functional groups present in the HAP coatings was carried out using a Fourier Transform Infrared (FT-IR) spectrophotometer instrument (IRAffinity-1, SHIMADZU). FT-IR spectra were recorded in the range of 400–4000 cm^{-1} with a resolution of 4 cm^{-1}. The deposited films were scraped off as powders from the substrate and mixed with KBr powder (80% in weight) to form an infrared transparent pellet.

The microstructural changes and the elements present at the surface of the coated specimen were studied by means of a scanning electron microscope equipped with energy dispersive X-ray spectroscope (SEM/EDS FTI QUANTA 200, detector SUTW-Sapphire, resolution: 135.25) using the standard EDAX ZAF quantification method on the SEC factor. The SEM was used to examine the morphological features of the coatings. Samples were mounted on individual substrate holders using a carbon adhesive tape.

Both coating thickness and coating roughness were measured using a profilometry analysis "DEKTAK 150 SURFACE PROFILERT". The surface of the coating is scanned at an interval of 1000–8000 μm. Three different areas were scanned and measured to determine a mean value for the thickness and the roughness parameter.

Nanoindentation experiments were performed with a Nano Indenter XP ™ (MTS Nano Instruments) employing a Berkovich diamond indenter. The samples were fixed on a metallic support using the heat softening glue crystalbond 509. 25 indentation tests were conducted randomly on the surface of the material with the same indentation testing conditions. The maximum indentation depth reached by the indenter was fixed at 2000 nm and the strain rate was equal to 0.05 s^{-1}. The instrument was operated in the continuous stiffness measurement (CSM) mode allowing the computation of the elastic modulus and the hardness continuously during the indentation loading. The harmonic displacement was 2 nm and the frequency was 45 Hz. The elastic modulus of the coating, E_C, is deduced from the reduced modulus, E_{RC}, given by the instrument, which takes into account the elastic properties, E_i

and ν_i, related to the indenter material and the Poisson's ratio of the coating, ν_C:

$$E_C = (1-\nu_C^2)\left[\frac{1}{E_{RC}} + \frac{(1-\nu_i^2)}{E_i}\right]^{-1} \quad (1)$$

For a diamond indenter, the elastic modulus, E_i, and the Poisson's coefficient, ν_i, are equal to 1140 GPa and 0.07, respectively [24]. ν_C is taken equal to the mean value of 0.3 because the analysis deals with a multilayered coating.

Unfortunately for thin films, the substrate can interfere with the mechanical property measurement. Consequently, a model must be applied for separating the influence of the substrate on the measurement. In the case of porous coating, Hemmouche et al. [25] have tested numerous models related to the elastic modulus determination of thin films. They conclude that the model of Gao et al. [26] leads to the best prediction and that it has the advantage of being independent of any fitting parameter. When the indentation depth increases, the measured reduced modulus, E_{RC}, changes gradually between two limits: E_{RF} (obtained for the lowest loads and representing the reduced modulus of the film) to E_{RS} (obtained for the highest loads and representing the reduced modulus of the substrate). This relative variation of the elastic modulus is expressed as a weight function Φ:

$$\frac{|E_{RC}-E_{RS}|}{|E_{RF}-E_{RS}|} = \Phi. \quad (2)$$

The weight function, based on the analytical solution of the contact of a rigid cylindrical indenter with an elastic layered body, takes the following form:

$$\Phi = \frac{2}{\pi}\arctan\left(\frac{t}{a}\right) + \frac{1}{2\pi(1-\nu)}\left[(1-2\nu)\frac{t}{a}\ln\left(1+\left(\frac{a}{t}\right)^2\right) - \frac{\frac{a}{t}}{1+\left(\frac{a}{t}\right)^2}\right]. \quad (3)$$

Here $a = h.\tan\Psi$, is the contact radius of an equivalent conical indenter at the maximum load and $\Psi = 70.3°$, corresponding to the half-angle of the tip conical indenter, h is the indentation depth, ν is the Poisson's coefficient of the specimens and equal to 0.3·t is the film thickness.

The adhesion of the coating was evaluated using a scratch tester (Millennium in accord with Standard ISO/EN 1071-3) with a spherical Rockwell C diamond indenter of 200 μm in radius. The scratch tests were performed on the coating by applying the load, which increases monotonously at the loading rate of 10,000 mN/min, whereas the specimen was shifted at the constant speed of 1500 μm/min. The applied force immediately starts to increase linearly with time. These conditions lead to a total scratch length of 1500 μm. The load at which the coating was removed from the substrate is referred to as the critical load (Lc). The scratch track was observed using an optical microscope. Five tests for each sample were recorded.

The corrosion behavior of the samples was evaluated by potentiodynamic cyclic voltammetry tests employing a Voltalab equipment (Serial: 913 V708/INT), interfaced with a computer and loaded with VoltaMaster 4 software in simulated human body fluid (SBF) at 37 ± 1 °C. The SBF solution is prepared using Kokubo and Takadama's formulation [27]. Before conducting the corrosion studies, the specimens were immersed in the SBF solution for 1 h in order to stabilize the system. Moreover, a renewed solution was used for each experiment. The exposed area of the samples in the SBF solution was 1 cm^2. A platinum electrode was used as the auxiliary electrode and the saturated calomel electrode (SCE) was used as the reference electrode. Corrosion potential (E_{Corr}), and corrosion current density (I_{Corr}) were determined using the Tafel diagram with sweeping potential from −1000 to +1000 mV at the rate of 1 mVs^{-1}, all the tests were carried out on several samples and, at least, three similar results were required to ensure reproducibility.

3. Results and discussion

3.1. Influence of annealing temperature and deposition parameters on the HAP coatings

Fig. 1 shows the surface of the HAP coatings prepared with different dipping rates at the same annealing temperature. As a result, the sample treated at 600 °C reveals the morphology of the coating, which differs according to the dipping rate, as shown in the different micrographs. The coating prepared at 10 mm/min (Fig. 1a) was distinctly composed of partially melted droplets. The coating shown in Fig. 1b was obtained by dipping with a withdrawal rate of 30 mm/min. It shows the heterogeneous aspect of the surface. The coating shown in Fig. 1**c**, prepared at 50 mm/min, is less rough and less complex as compared to the previous ones. For the lowest dipping rate (10 mm/min), extensive cracking was observed, whereas for the highest one (50 mm/min), the surface exhibited uniform morphology. The coating prepared at 50 mm/min, annealed at 700 °C − 60 min (Fig. 1d) and the coating prepared at 50 mm/min, annealed at 750 °C − 60 min (Fig. 1e), allow for the observation of the annealing treatment influence. At 700 °C, the surface of the coating appears dense and homogeneous. At the highest temperature of 750 °C, cracks and defects are visible thus indicating that severe solvent evaporation has occurred. The annealing treatment leads to a contraction of the coating volume, which damages the structural integrity by formation of micro-cracks on the surface. By applying a low annealing temperature of 500 °C and a dipping rate of 80 mm/min, as shown in Fig. 1f, uniform morphology was obtained, which is characterized by a homogeneous and smooth appearance. This indicates that solvent evaporation was reduced.

In Fig. 2, the XRD patterns for coating (a), prepared at 50 mm/min, 700 °C − 60 min (see Fig. 2a) and coating (b), prepared at 50 mm/min, 600 °C − 60 min (see Fig. 2b), show peaks for which the positions and widths correspond to a crystallized HAP structure (PDF no. 00-009-0432). The HAP characteristic triplet peaks at (211), (112) and (300) planes are observed for 2θ values between 31° and 33°. Since the coatings are relatively thinner, around 2 μm, the X-ray diffraction patterns in Fig. 2 present large peaks related to the diffraction of the crystallographic structure of the 316 L stainless steel substrate (PDF no. 00-006-0694). However, additional peaks can be detected. For the samples annealed at 600 °C and 700 °C, the peak observed at 2θ = 33.1° corresponds to the presence of the Fe_2O_3 phase (PDF no. 00-024-0072), whereas the peak observed at 2θ = 36.82° corresponds to the presence of the Fe_3O_4 phase (PDF no. 00-026-1136). The peak located at 2θ = 35.6° associated to the $FeCr_2O_4$ phase (PDF no. 01-071-4917) is only detected in the coating treated at 700 °C. The XRD patterns indicate the formation of a composite layer of iron with HAP, which results from the oxidation of the base metal and its diffusion toward the outer surface. The formation of metal oxides at the surface is due to the oxidation of the substrate reacting with the atmosphere. The major HAP peaks were detected and indexed along with the iron peaks. Other calcium phosphate phases on the coatings were absent. Aging of the precursor solution has been found to be critical in developing an apatitic phase and specific aging time period either at room or higher temperature is necessary to form a phase-pure apatite [28]. Gross et al. [29] have demonstrated that a time of 24 h is necessary for a complete combination of the calcium and phosphorus precursors to produce a hydroxyapatite coating.

The XRD patterns of the coating shown in Fig. 1**c**, prepared at 80 mm/min and annealed at 500 °C for 60 min (see Fig. 2c), show several peaks related to the HAP phase. The structure can be considered quasi pure and partially crystalline. This crystallization temperature of 500 °C is characteristic of amorphous calcium phosphates. Previous work [29] performed on HAP coatings deposited by a spin coating method showed that crystallization of the hydroxyapatite occurs between

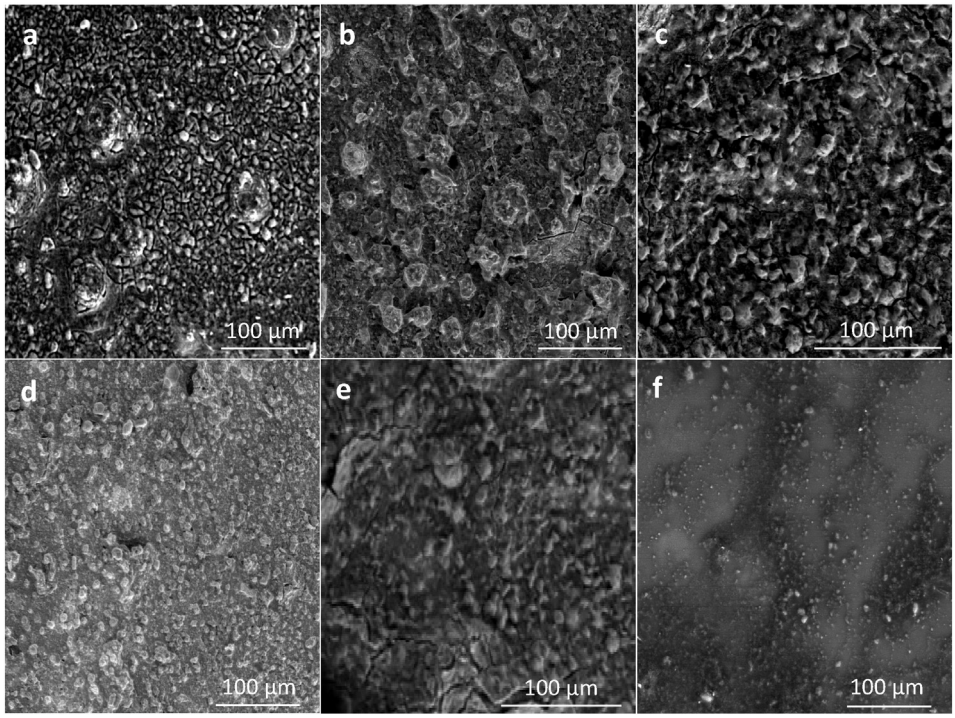

Fig. 1. SEM observations of the HAP coatings surfaces prepared with dipping rate and annealing treatment, respectively of: a) 10 mm/min, 600 °C — 60 min, b) 30 mm/min, 600 °C — 60 min, c) 50 mm/min, 600 °C — 60 min, d) 50 mm/min, 700 °C — 60 min, e) 50 mm/min, 750 °C — 60 min, and f) 80 mm/min, 500 °C — 60 min.

500 and 600 °C, so authors preferred annealing the coating at 500 °C for 5 min in order to remove most of the organics and then complete the treatment by a final firing at 800 °C for 10 min. This allows the removal of the remaining organic constituents required for the formation of a homogeneous thin hydroxyapatite coating. However, it was shown here, from SEM and XRD analysis, that a dipping rate of 80 mm/min and a temperature of 500 °C for 60 min were the optimum conditions for the production of crack free pure hydroxyapatite coatings. In the following, only the HAP coatings obtained under these conditions will be studied.

The FT-IR spectrum of the HAP coatings prepared at a dipping rate of 80 mm/min and annealed at 500 °C for 60 min is indicated in Fig. 3. This figure shows well-defined bands associated with the presence of PO_4 groups at 473, 563 and 600 cm^{-1} [30]. The trace at 473 cm^{-1} is attributed to the ν_2 bending vibration. The triply degenerated ν_4 bending vibrations are reflected as traces at 563 and 600 cm^{-1}. The band at 964 cm^{-1} corresponds to ν_1 and the bands at 1049 and 1089 cm^{-1} correspond to the ν_3 vibrations of PO_4^{3-} ions. The broad and high-intensity band extending from 2500 to 3600 cm^{-1} derives from the ν_3 and ν_1 stretching mode of the hydrogen-bonded H_2O molecules and the band at 1632 cm^{-1} derives from the ν_2 bending mode of the H_2O molecules. The bands at 3572 and 630 cm^{-1} arise from the stretching and vibrational modes, respectively, of the OH^- ions in the hydroxyapatite structure [31].

The locations of the carbonate peaks in the FT-IR pattern are indicated at the bands of 1419, 1460, 1501, 1540 cm^{-1} and a singlet at 873 cm^{-1}. The presence of the carbonate group in the apatite structure

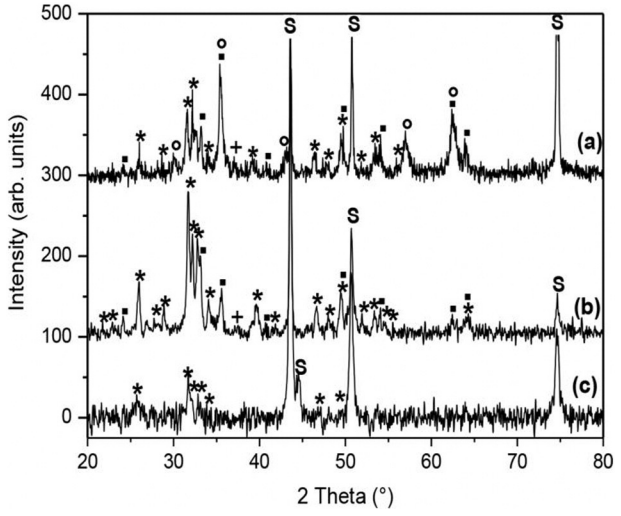

Fig. 2. XRD patterns of the different HAP coatings formed on the 316 L SS: (a) 50 mm/min, 700 °C — 60 min, (b) 50 mm/min, 600 °C — 60 min, (c) 80 mm/min, 500 °C — 60 min. (■) Fe_2O_3, (+) Fe_3O_4, (°) $FeCr_2O_4$, (*) Hydroxyapatite, and (S) Substrate.

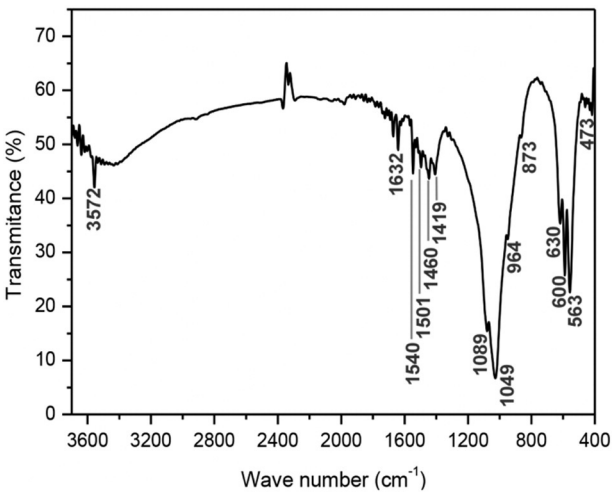

Fig. 3. FT-IR analysis of the optimized HAP coating deposited at the rate of 80 mm/min and annealed at 500 °C for 60 min.

corresponds to the partial substitution of OH^- and PO_4^{3-} groups, forming carbonated apatite [30,32–34]. The reaction was performed in open air that caused incorporation of a small amount of CO_3^{2-} ions in the formed HAP particles. The source of the carbonate was due to the absorption of atmospheric CO_2 into the ethanol solution. Carbonate ion is produced by the reaction of CO_2 with water and OH^- as follows [35]:

$$CO_2 + 2H_2O \leftrightarrow H_2CO_3 + H_2O$$
$$H_2CO_3 + OH^- \leftrightarrow HCO_3^- + H_2O$$
$$HCO_3^- + OH^- \leftrightarrow CO_3^{2-} + H_2O.$$

The coatings can then be considered as a carbonated apatite. The FT-IR spectrum from the present study is similar to that reported by Yala et al. [36] who synthesized the hydroxyapatite using a similar sol–gel processing route.

3.2. Effect of TiO_2 sub-layer on the microstructural characteristics of the HAP coatings

3.2.1. SEM images

The surface morphology of the HAP–TiO_2 bilayer coating is shown in Fig. 4(a) and (b). SEM surface examination reveals no detectable cracks and an absence of pores for this coating. When TiO_2 was deposited onto the 316 L stainless steel substrate (Fig. 4b), initial machining grooves on the substrate could be observed, thus suggesting the formation of a very smooth TiO_2 layer. The HAP outer layer reproduces the surface features of the TiO_2 underlying film. According to profilometry measurements, each layer had uniform thickness. Fig. 4c is the magnification surface of the HAP coating presented in Fig. 1e. The single HAP layer has a discontinuous structure as compared to the bilayer HAP–TiO_2 coating (Fig. 4b). The morphology of the surface indicates that the HAP coating is composed of pores having a spherical shape and presents irregular agglomerates. According to Rajabi-Zamani et al. [32] and Feng et al. [37], the agglomerated structure is due to the aging period. After deposition of the HAP coating over the TiO_2 layer, the surface changed and exhibited a relatively rough structure (Fig. 4b and c). Both surface roughness and thickness were estimated according to the profilometry analysis and the parameters are summarized in Table 1. The thickness of the HAP layer and HAP–TiO_2 bilayer were approximately of 1600 and 1019 nm, respectively. The surface roughness of the HAP layer coated-316 L substrate decreased from about 1310 to 95 nm after the introduction of the TiO_2 sub-layer at the surface of the 316 L stainless steel substrate. The values of the thickness and roughness of the TiO_2 coating were 300 nm and 43 nm, respectively, thus confirming the smoothness of this coating.

3.2.2. X-ray diffraction patterns

XRD patterns of the TiO_2, HAP and HAP–TiO_2 coatings are shown in Fig. 5. The XRD pattern of the TiO_2 layer deposited on the 316 L SS substrate is given in Fig. 5a. The XRD analysis reveals a crystalline structure of anatase (PDF no. 00-004-0477). All the peaks correspond to the TiO_2 phase besides the reflections from steel substrate. The diffraction pattern observed for the HAP–TiO_2 coating is given in Fig. 5b. It consists of sharp peaks attributed to the substrate 316 L stainless steel. Several major peaks correspond to the HAP and anatase structures, suggesting that there is no phase transformation, which can be caused by the simultaneous calcinations of the HAP and TiO_2 layers. Compared to the HAP coating directly deposited on the 316 L substrate without the TiO_2 layer (Fig. 2c), the hydroxyapatite peak intensities increased, indicating that there was an improvement in crystallization.

3.2.3. Elemental analysis by EDS

As shown in Table 2 ("EDAX ZAF Quantification Standardless SEC Table"), together with the element composition analysis of the coatings and 316 L stainless steel substrate, it can be noticed that no elements

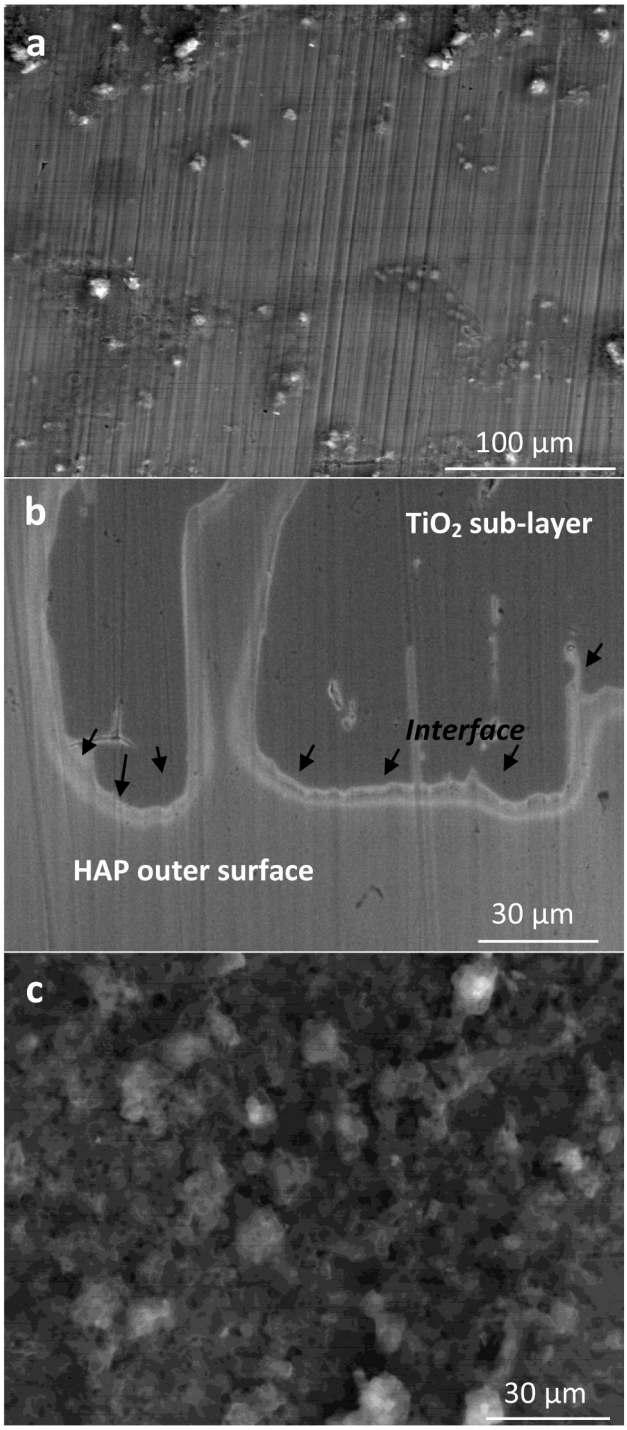

Fig. 4. SEM images of: (a) HAP–TiO_2 bilayer coating, and (b) the interface of the HAP coated on the TiO_2 interlayer, (c) HAP single coating.

Table 1
Structural and corrosion parameters of the uncoated and ceramics coated 316 L stainless steel.

	Thickness (nm)	Roughness (nm)	E_{Corr} (mV)	I_{Corr} (µA cm^{-2})
HAP–TiO_2	1019	95	−234	0.089
TiO_2	300	43	−373	0.630
HAP	1600	1310	−460	0.860
Substrate	–	–	−665	1.000

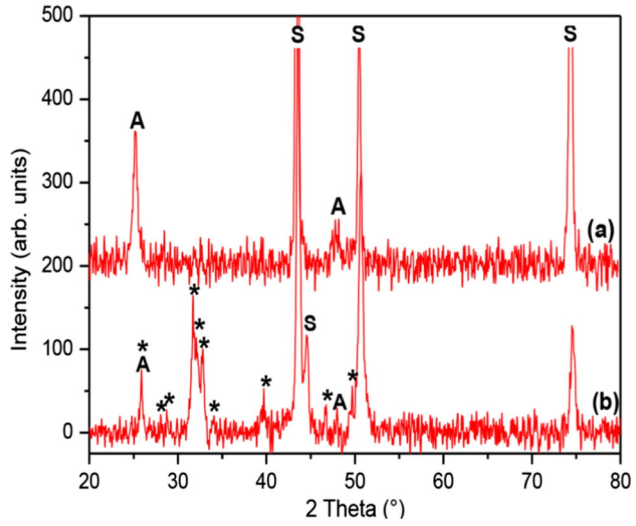

Fig. 5. XRD patterns of (a) TiO_2, and (b) HAP–TiO_2 coatings. (*) Hydroxyapatite, (A) anatase, and (S) Substrate.

other than those expected for the TiO_2, HAP and 316 L stainless steel substrate were detected. The lower quantity of Ti in the HAP–TiO_2 bilayer coating indicates the existence of Ti at the interface of the HAP–TiO_2 system and therefore, the presence of the TiO_2 oxide as a sub-layer of the hydroxyapatite coating. Moreover, EDS analysis indicates the presence of carbon in the HAP coating. According to FT-IR analysis, the HAP coating contains a small amount of carbon resulting from the carbonate substitution of phosphate. From Table 2, the Ca/P molar ratio was equal to 1.77. A higher Ca/P ratio in hydroxyapatite film was believed to be related to the carbonate substitution of phosphate, as revealed by the FT-IR analysis. It is usually expected that the absorption of the CO_3^{2-} peaks is more pronounced when the Ca/P ratio is greater than the stoichiometric value [38]. The nonstoichiometric Ca/P ratio resulted from carbonate substitution for phosphate, as well as a poorly developed crystal structure.

The HAP coating resulting from the 500 °C annealing treatment gave rise to a nonstoichiometric carbonated (CHAP) apatite. A high degree of crystallinity and chemical stability has been included among the required properties of an ideal hydroxyapatite [39]. However, a low degree of crystallinity associated to a high resorbability is also effective for promoting early bone growth [40].

3.3. Hardness and elastic modulus of the uncoated and HAP, TiO_2, HAP–TiO_2 coated 316 L stainless steel systems

25 nanoindentation tests have been performed randomly on the surface of the substrate and of the different coated materials in order to obtain representative variations of the hardness as a function of the indenter displacement. Fig. 6 represents the hardness variation for the different situations. As it is clearly shown on this figure, the uncoated substrate presents the highest hardness value with a hardness variation, which decreases from 7 GPa, close to the external surface, to 3 GPa toward the core of the material for the highest indenter displacements. The increase in hardness toward the surface can be explained by the presence of oxides such as hematite-Fe_2O_3 and magnetite-Fe_3O_4 on the substrate, which is very reactive with the atmosphere mainly when it is exposed to temperatures higher than 600 °C (see Fig. 2). On the other hand, Chicot et al. [41] have studied various iron oxides by means of molecular dynamic analysis (MDA) and instrumented indentation. They concluded that the two techniques lead to the same prediction of the mechanical properties of these oxides, i.e. 6.3 GPa for the hardness of magnetite and 8.2 GPa for the hardness of hematite, the elastic modulus being more or less constant close to 190 GPa. These values obtained for the oxides can explain the hardness gap since the hardness values of these oxides are in good agreement with the experimental value of 6.7 GPa determined on the surface of the substrate.

For the TiO_2 coating, we note that the hardness is very similar to that of the substrate except for indenter displacements very close to the outer surface, typically over the first 150 nm in depth. In this region, we applied the model of Jönsson and Hogmark [42] for determining the hardness of the film only. In this model, the measured hardness, called "composite hardness" H_C, depends on the hardness of the coating H_F, and the hardness of the substrate H_S as follows:

$$H_C = H_S + \left(2C\frac{t}{d} - \left(C\frac{t}{d}\right)^2\right)(H_F - H_S). \quad (4)$$

Here t is the film thickness, d is the indent diagonal and C a constant which takes a value between 0.5 and 1, depending on the mechanical behavior of the tested material. C equals 0.5 for brittle materials and 1 for ductile materials. Moreover,

$$d = 2tg74\ h. \quad (5)$$

Here h is the indentation depth.

Applied to the hardness variation of the TiO_2 films and using the hardness values of the substrate, we obtained a value of 3.5 GPa for the hardness of the titania oxide. For information, Fu et al. [43] indicate that the hardness of titania films can vary to a great extent, between 2

Table 2
Energy dispersive X-ray quantification of the HAP, TiO_2, and HAP–TiO_2 coatings.

Element	C	O	Ni	P	Ca	Cr	Fe	Ti
Hydroxyapatite coating								
Weight fraction (wt.%)	06.06	33.03	01.65	13.57	31.06	02.06	12.57	–
Atomic fraction (at %)	12.33	50.44	00.69	10.70	18.93	01.42	05.50	–
Titania film								
Weight fraction (wt.%)	–	17.23	09.21	–	–	05.97	22.59	45
Atomic fraction (at %)		40	05.83	–	–	04.27	15	34.90
Hydroxyapatite–titania bilayer coating								
Weight fraction (wt.%)	04.98	35.90	02.48	08.64	16.86	06.22	22.44	2.48
Atomic fraction (at.%)	12.01	54.09	01.02	06.72	12.33	02.89	09.69	1.25

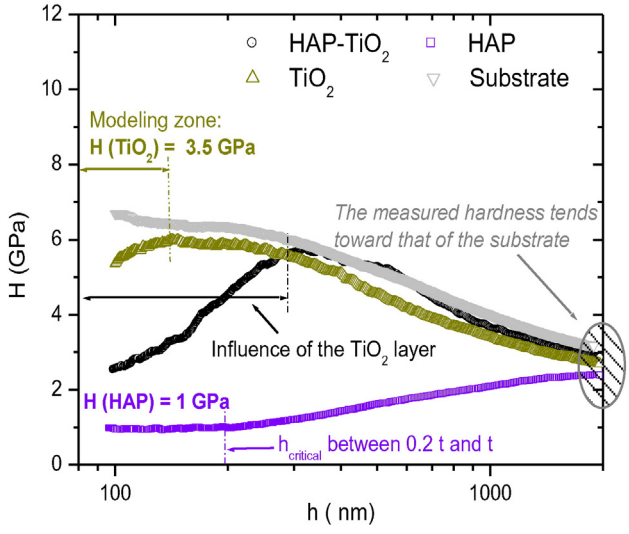

Fig. 6. Hardness versus the indenter displacement obtained by using the CSM mode of nanoindentation performed on the uncoated substrate, the HAP, TiO_2, and HAP–TiO_2 coatings.

and 18 GPa measured by nanoindentation, depending on crystalline nature and microstructure of the films [44,45].

For the HAP coating, the hardness is found to be much lower at the extreme surface. We can note that the hardness value is constant for the lowest indenter displacements over 200 nm in depth. In this region, the hardness is close to 1 GPa. After 200 nm in depth, the hardness value increases toward a value of 3 GPa which corresponds to the hardness of the steel substrate. In this zone, the substrate interferes with the hardness measurement. For this coating, no application of model is required since the film hardness has been determined for the lowest displacements of the indenter. Indeed, the hardness has a constant value of 1 GPa for indenter displacements between 100 and 200 nm.

For the HAP–TiO_2 coating, it is interesting to note that the hardness value varies between two limits corresponding to the HAP hardness and the substrate hardness, respectively for the lowest and highest indenter displacements. Between these two limits, the benefit of the sub-layer of TiO_2 in terms of mechanical properties is clearly visible since the hardness variation is observed between 2.5 GPa at the extreme surface, as compared to only 1 GPa for the HAP coating, until 6 GPa corresponding to the TiO_2 coating or steel substrate hardness at only 300 nm. As a conclusion, we showed that the TiO_2 sub-layer significantly improves the hardness of the HAP coating. In [12] it is shown that the microhardness of the HAP coating, which is about of 459 HV (4.50 GPa) increases with the addition of the TiO_2 and SiO_2 inner layers, to reach approximately 530 HV (5.19 GPa) for the global HAP bilayer coatings. In addition, the hardness values obtained from both classic tests in microindentation and the continuous stiffness measurement mode in nanoindentation are slightly different. This is due to the fact that nanoindentation is more sensitive to the surface roughness and the influence of defects, which could be present in the material. Moreover, nanoindentation is the most useful method to separate the contribution of each layer in the bilayer coatings.

As already mentioned by [17–20], the substrate can interfere with the elastic modulus measurement for the lowest indenter displacements at the beginning of the indentation, as can be observed in Fig. 7. Subsequently, we have applied the model of Gao et al. [26] on the complete range of indentation data (Fig. 7). The elastic modulus is then represented as a phi-function for the TiO_2, HAP and HAP–TiO_2 coatings. All the values for the composite elastic modulus seem to be adequately represented by a unique straight line for the homogeneous TiO_2 and HAP coatings. In Fig. 7a and b, the two straight lines tend toward the value of 190 GPa related to the elastic modulus of the substrate when Φ is null, whereas that of the film is obtained when this latter parameter equals 1. As a result, the elastic moduli of the films are equal to 60 GPa for the TiO_2 coating and 6 GPa for the HAP coating. For the HAP–TiO_2 coating for which the elastic modulus of the film tends toward 30 GPa, we distinguish two zones depending on the value of the weight function. When Φ is lower than 0.5, the HAP film has no real influence on the elastic modulus variation since the indentation data can be adequately represented by the straight line related to the TiO_2 coating (Fig. 7a), which tends toward 60 GPa when Φ equals 1. When Φ is higher than 0.5, the presence of the HAP coating leads to a change of the elastic modulus variation and the measured elastic modulus decreases compared to the straight line and its value tends toward that of the HAP coating, that is to say a value slightly higher than 30 GPa.

As a conclusion on the mechanical properties of the different coatings studied in this work, the elastic modulus and the hardness of the single hydroxyapatite coating were found to be equal to 6 and 1 GPa, respectively. The above confirms the fact that the as-deposited HAP coatings have relatively poor mechanical properties. For the TiO_2 coating, the values of the elastic modulus and the hardness reach 60 and 3.5 GPa, respectively. For the bilayer coatings, these values are intermediate since we obtained 30 and 2.5 GPa, respectively. This result confirms the interest from a mechanical point of view of the introduction of an intermediate layer having better mechanical properties than the HAP coating alone.

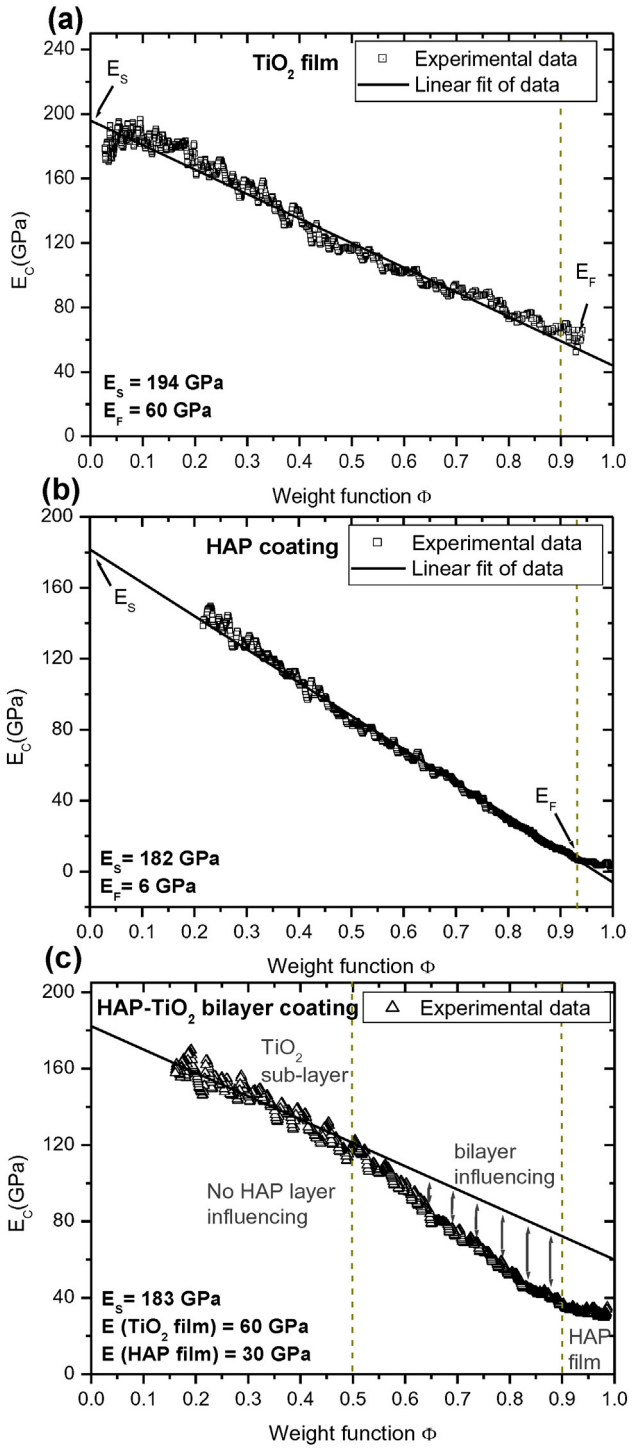

Fig. 7. Model of Gao et al. [26] applied on the indentation data obtained from nanoindentation tests performed on the (a) TiO_2, (b) HAP, and (c) HAP–TiO_2 coatings.

Some works have shown that the mechanical properties of hydroxyapatite depend on the structural characteristics such as porosity, crystallinity, particle size, and being different for the same material arising from different processing histories. Since apatite is more commonly found as nanocrystals, nanoindentation studies on single crystals of hydroxyapatite can provide important information on the hardness and the elastic modulus for HAP materials used in biomedical applications. The mechanical properties of these materials depend on the orientation of the crystals [46,47]. The values for the hardness and elastic modulus obtained by Saber-Samandari et al. [47] on a natural single crystal of

hydroxyapatite revealed higher values for the base, 7.1 and 150.4 GPa, as compared to the side, 6.4 and 143.6 GPa, respectively. Longer crack lengths were observed on the base compared to the side under the same applied load. These results suggest that the HAP crystal has a higher resistance to micro-cracking on the side, which is useful for the bone, while exposing the base is preferable to minimize mass loss from abrasion with the teeth. These mechanical properties of single crystalline hydroxyapatite are higher as compared to those reported here. Indeed, both the hardness and elastic modulus values measured on sol–gel hydroxyapatite coatings are very low. We can assume that the crystal shape, size and arrangement of the hydroxyapatite particles are responsible for the higher mechanical properties. Thereby, the additive effect of the anatase TiO_2 crystalline film shows that the measured values of the hardness and the elastic modulus of the hydroxyapatite–titania double layer coating vary to a large extent.

On the other hand, nanoindentation experiments performed on the surface of thermal sprayed hydroxyapatite coatings consisting of well melted solidified splats, produced from small (20–40 μm), medium (40–60 μm) and large (60–80 μm) particle sizes powders [48] lead to some interesting concluding remarks. Indeed, the hardness and elastic modulus can be directly linked to the particle size. For example, the mechanical properties decrease when the particle size increases, i.e. 5.8 ± 0.6 and 121 ± 7 GPa for small particles size, 5.4 ± 0.5 and 118 ± 7 GPa for medium particles size and 5.0 ± 0.6 and 114 ± 7 GPa for the large particles size, respectively for the hardness and the elastic modulus. This decrease can be attributed to the de-hydroxylation of hydroxyapatite. However, these values are higher than those reported here. This shows the effect of the particle size and eventually the effect of the de-hydroxylation of hydroxyapatite on the mechanical properties of the coating. Moreover, the decrease in mechanical properties could be related to the pore content as has been shown by Gross et al. [49] by using micro- and nanoindentation experiments for the determination of the elastic modulus of the hydroxyapatite pellets sintered at 1200 °C for 2 h. These authors reported a decrease in elastic modulus from the value of 110 ± 10 GPa to 100 ± 10 GPa when the porosity fraction increases by 3%. This result agrees well with the conclusion presented here. It is assumed that the morphological and microstructural properties of the bilayer coating, which exhibits a crystallinity increase, a porosity fraction and a roughness decrease have played a major role in producing higher hardness and elastic modulus values.

The elastic modulus and hardness of the hydroxyapatite coatings are subsequently compared to the values given in the literature according to the synthesis conditions. For example, for a claimed HAP coating, Ou et al. [50] give values of elastic modulus ranging from 3.6 and 7 GPa. This hydroxyapatite coating was prepared through two processes: self-assembly in simulated body fluid and a hydrothermal method. The samples were then incubated in a dilute collagen solution for 24 h to produce the composite coatings. In this case, the elastic modulus of the hydroxyapatite coating was 3.6 GPa, which reaches 7.5 GPa after the collagen incubation treatment. Tsui et al. [39] used the vacuum plasma spraying technique and obtained a value of 5.5 GPa for the elastic modulus. However, a higher value of 60 GPa for the elastic modulus and 4 GPa for the hardness were given by Gross et al. [51] on a plasma sprayed coating. Vijayalaqshmi et al. [52] have annealed the as-prepared sol–gel HAP coatings at different temperatures and obtained the corresponding hardness of 1.2 GPa. Additionally, the titania elastic modulus calculated in this work for the annealing temperature of 450 °C is in good agreement with the elastic modulus values reported by Olofinjana et al. [53] who also used the sol–gel process. Their reported values were in the range of 55–65 GPa for the as-deposited film, whereas those reported for an annealing temperature of 550 °C are of approximately 85 GPa. In this study, the hardness is comparable with those reported previously for pure HAP ceramics (1.0–5.5 GPa), which are close to those properties of natural teeth [54]. The elastic modulus can be approximately compared with the average elastic modulus value provided by nanoindentation on human tibia cortical bone (E = 25.8 GPa) [55].

3.4. Scratch tests

Fig. 8(a_1–a_3) and (b_1–b_3) illustrate the scratch length images during the scratch force test of the HAP coating and the HAP–TiO_2 bilayer coating, respectively. The scratch direction was from left to right for all of the scratch images. The optical micrographs are representative of the phenomenon occurring at the surface of the coated systems under different loading amplitudes and indicate that several types of failure modes were present during the scratching of the hydroxyapatite layer on the titania-coated and uncoated substrates. It is possible to position them on loading graphs (Fig. 8(a) and (b)), which represent the load-displacement graphs and the corresponding photos (a_1–a_3 and b_1–b_3) to examine the different forms of damage induced by the indenter tip and to correlate them with the load applied.

As shown in Fig. 8(a_1) and (b_1), no visible wear debris were observed to come out from the films in the initial stage of small applied load (1915 mN) for the HAP coating and (1525 mN) for the HAP–TiO_2 coating. As the load was gradually increased to 2400 mN, the first cracks are observed on the scratch track of the HAP coating and delamination occurred on the trackside (Fig. 8(a_2)). As the load continued to increase (2925 mN), the trackside cracking and delamination became more severe and the coating was delaminated from the substrate along the scratch path. The corresponding load was recorded as the critical load Lc_1. For the bilayer HAP–TiO_2 coating, as shown in Fig. 8(b_2), no significant damage is observed on the scratching surface. The coating failures began to appear only after increasing the load to 5100 mN. Here the critical load (Lc_2) has to be determined from Fig. 8(b_3). The total detachment of the HAP coating from the substrate is clearly observed in Fig. 8(a_3). Finally, it can be seen from these graphs that the bilayer HAP–TiO_2 coating presents approximately a scratch length/displacement of 1050 μm and a critical load (Lc_2) of 6430 mN, whereas the single HAP coating exhibits approximately a scratch length/displacement of 510 μm and a critical load (Lc_1) of 2925 mN.

The improvement in bonding strength with the introduction of the TiO_2 bond was attributed to the enhanced of the chemical affinity of TiO_2 toward the HAP layer, as well as toward the 316 L stainless steel substrate. Based on these results, it could be confirmed that the bonding strength of the HAP bioceramic coating layer was highly dependent on the substrate surface. A better adhesion between the HAP layer with the TiO_2 layer is found as compared to its adhesion with the substrate [3,56]. The critical load for the failure of the coating from the substrate increased from 2925 mN to 6430 mN with the introduction of the titania sub-layer.

3.5. Corrosion test

Fig. 9 shows the potentiodynamic cyclic voltammetry curves of the HAP–TiO_2, TiO_2, HAP coated and uncoated 316 L SS systems, immersed in SBF solution. The corrosion parameters determined from these curves by the Tafel extrapolation method are summarized in Table 1. The corrosion parameters are corrosion potential (E_{Corr}), and corrosion current density (I_{Corr}). The potentiodynamic curve, for the HAP–TiO_2 coating shifted to the right when compared to HAP, TiO_2 coated and uncoated substrate curves. Results of electrochemical tests reveal the influence of the different coatings on the corrosion resistance of the 316 L stainless steel. The lower I_{Corr} value for the HAP–TiO_2 coated system indicates that it is more corrosion resistant than the HAP and TiO_2 coated systems, which are, nevertheless, more resistant than the uncoated substrate.

The potentiodynamic curve of HAP–TiO_2 coated 316 L stainless steel substrate was noticeably different from that of the HAP coated 316 L stainless steel substrate, indicating that the titania film produces a real effect on the corrosion behavior. The TiO_2 coating reduces both the corrosion potential and current density. The application of the TiO_2 sublayer on the 316 L stainless steel causes an improvement in the corrosion resistance, which can be due to the good adhesion of the HAP–TiO_2–316 L stainless steel substrate system. The TiO_2 film acts as a

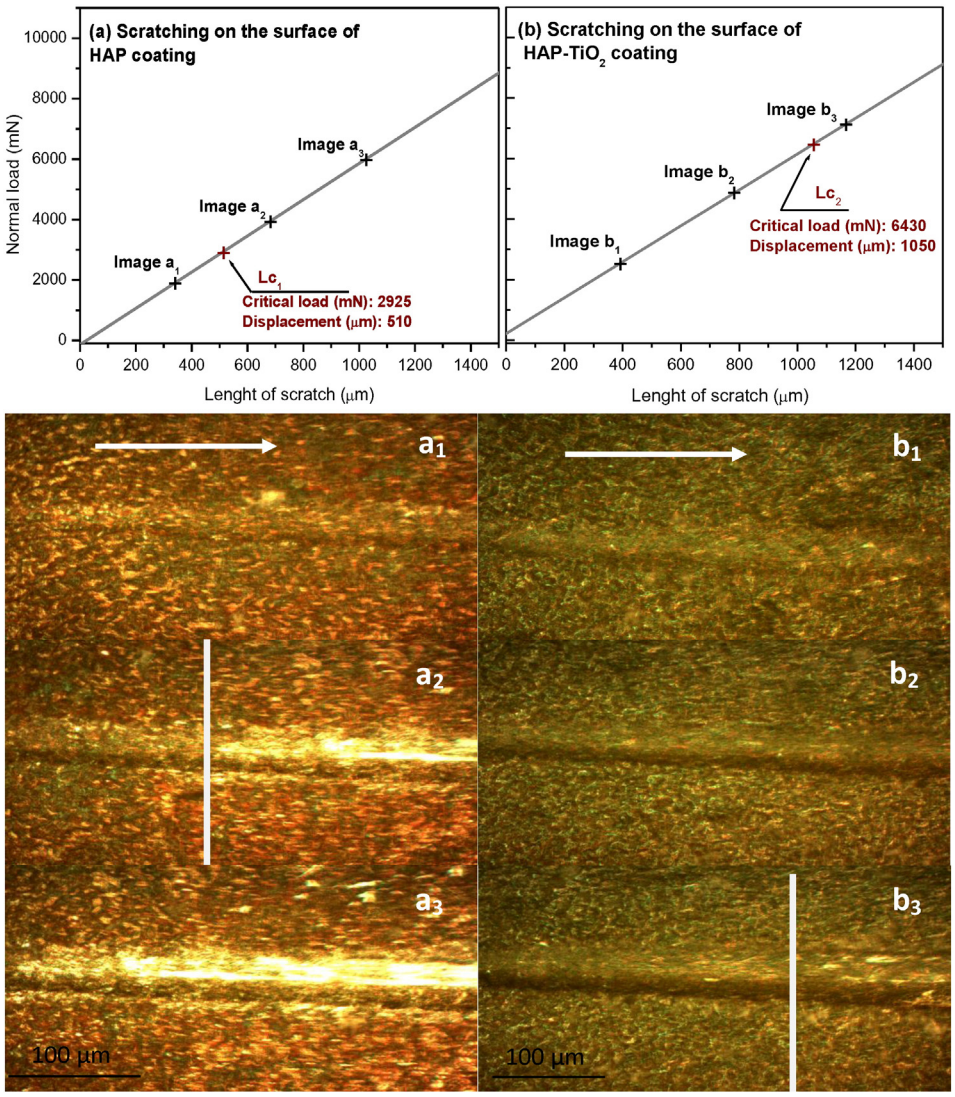

Fig. 8. Load-displacement graphs of the scratch test realized on (a) HAP, (b) HAP–TiO_2 coatings and optical micrographs (a_1–a_3, b_1–b_3) representative of the HAP, HAP–TiO_2 surface damage, respectively, arising from scratch tests (load progressively increasing from left to right indicated by the white arrow). The white bars inserted are referred to as the critical load (Lc_1 and Lc_2).

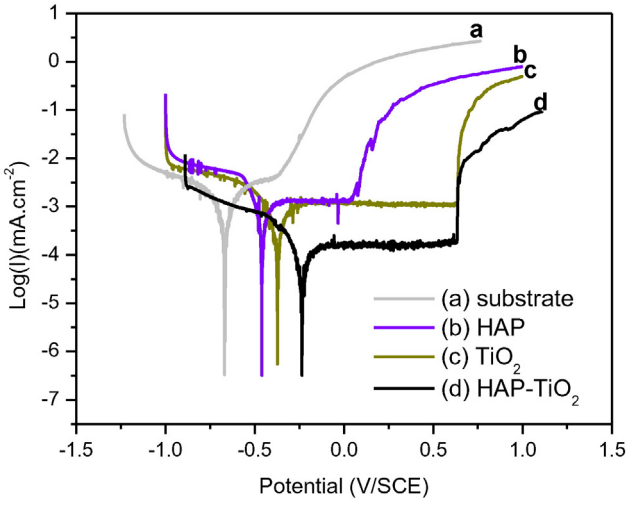

Fig. 9. The potentiodynamic curves of the uncoated 316 L stainless steel substrate, and the HAP, TiO_2, HAP–TiO_2 coated systems in SBF solution.

barrier and it blocks the porosity of the outer HAP coating as revealed by the microstructural investigation. The titania film and the hydroxyapatite layer provide double protection for the steel substrate.

This study clearly shows the contribution of TiO_2 inner layer on 316 L stainless steel on the morphological, structural and mechanical properties, but also, on the adhesion strength and the corrosion behavior of the hydroxyapatite. This will assist further improvements of HAP materials used in biomedical applications. Introduction of different oxides such as silica, alumina, etc. as inner layers between the substrate and the HAP coating will be of interest to the properties of the layered coating and will contribute to the function of the biomaterial.

4. Conclusions

Prior to HAP coating, a titania thin film was pre-coated onto the 316 L stainless steel substrate at 450 °C for 60 min. According to the microstructural analysis, the HAP coated on the TiO_2-substrate system at the temperature of 500 °C is dense and crystalline compared to the HAP single coating.

The effect of the structure and morphology on the mechanical properties of HAP after the introduction of a TiO_2 sub-layer has been investigated. The comparison between the elastic modulus and hardness of the

HAP and the bilayer HAP-TiO_2 systems reveals the existence of a significant gap, which indicates the benefit of the TiO_2 intermediate layer prior to HAP deposition. In addition, the introduction of the titania film significantly improved the bonding strength of the HAP layer to the 316 L stainless steel substrate. The double HAP–TiO_2 coatings have higher corrosion resistance than the single HAP coating and the uncoated 316 L stainless steel substrate.

As a concluding remark, the morphological and structural characteristics of the hydroxyapatite bilayer coating depend on the surface features of the underlying substrate before and after the deposition of the TiO_2 oxide layer. The deposition of the TiO_2 sub-layer gives rise to the formation of a different type of hydroxyapatite coating. This represents an advantage for various applications of the hydroxyapatite bioceramic in the medical field.

References

[1] J. Blumn, K.L. Eckert, A. Schroeder, M. Petitmermet, S.W. Ha, E. Wintermantel, In vitro testing of porous titanium dioxide ceramics, in: T. Kokubo, T. Nakamura, F. Miyaji (Eds.), Proceedings of the 9th International Symposium on Ceramics in Medicine, Otsu, Japan 1996, p. 89.

[2] S. Nagarajan, N. Rajendran, Surface characterisation and electrochemical behaviour of porous titanium dioxide coated 316 L stainless steel for orthopedic applications, Appl. Surf. Sci. 255 (2009) 3927–3932.

[3] H.W. Kim, Y.H. Koh, L.H. Li, S. Lee, H.E. Kim, Hydroxyapatite coating on titanium substrate with titania buffer layer processed by sol–gel method, Biomaterials 25 (2004) 2533–2538.

[4] C.E. Wen, W. Xu, W.Y. Hu, P.D. Hodgson, Hydroxyapatite/titania sol–gel coatings on titanium–zirconium alloy for biomedical applications, Acta Biomater. 3 (2007) 403–410.

[5] W. Xu, W.Y. Hu, M.H. Li, Q.Q. Ma, P.D. Hodgson, C.E. Wen, Sol–gel derived HA/TiO2 double coatings on Ti scaffolds for orthopedic application, Trans. Nonferrous Metals Soc. China 16 (2006) 209–216.

[6] T.P. Singh, H. Singh, H.H. Singh, Characterization, corrosion resistance, and cell response of high-velocity flame-sprayed HA and HA/TiO_2 coatings on 316 L SS, J. Therm. Spray Technol. 21 (2012) 917–927.

[7] P.C. Rath, L. Besra, B.P. Singh, S. Bhattacharjee, Titania/hydroxyapatite bi-layer coating on Ti metal by electrophoretic deposition: characterization and corrosion studies, Ceram. Int. 38 (2012) 3209–3216.

[8] D.M. Liu, T. Troczynski, W.J. Tseng, Water-based sol–gel synthesis of hydroxyapatite: process development, Biomaterials 22 (2001) 1721–1730.

[9] A. Montenero, G. Gnappi, F. Ferrari, M. Cesari, E. Salvioli, L. Mattogno, S. Kaciulis, Sol–gel derived hydroxyapatite coatings on titanium substrate, J. Mater. Sci. 35 (2000) 2791–2797.

[10] P. Li, K. de Groot, Better bioactive ceramics through sol–gel processJ. Sol–Gel Sci. Technol. 2 (1994) 797-801.

[11] D.B. Haddow, P.F. James, R. van Noort, Characterization of sol–gel surfaces for biomedical applications, J. Mater. Sci. Mater. Med. 7 (1996) 255–260.

[12] D. Sidane, H. Khireddine, S. Yala, S. Ziani, F. Bir, D. Chicot, Morphological and mechanical properties of hydroxyapatite bilayer coatings deposited on 316 L SS by sol–gel method, Metall. Mater. Trans. B 46 (2015) 2340–2347.

[13] A. Iost, G. Guillemot, Y. Rudermann, M. Bigerelle, A comparison of models for predicting the true hardness of thin films, Thin Solid Films 524 (2012) 229–237.

[14] E.S. Puchi-Cabrera, A new model for the computation of the composite hardness of coated systems, Surf. Coat. Technol. 160 (2002) 177–186.

[15] H. Buckle, Applications to other material properties, in: J.W. Westbrook, H. Conrad (Eds.), The Science of Hardness Testing and its Research Applications, ASM, Metals Park, OH 1973, pp. 453–491.

[16] Y. Sun, T. Bell, S. Zheng, Finite element analysis of the critical ratio of coating thickness to indentation depth for coating property measurements by nanoindentation, Thin Solid Films 258 (1995) 198–204.

[17] T. Chudoba, N. Schwarzer, F. Richter, Steps towards a mechanical modeling of layered systems, Surf. Coat. Technol. 154 (2002) 140–151.

[18] F. Cleymand, O. Ferry, R. Kouitat, A. Billard, J. von Stebut, Influence of indentation depth on the determination of the apparent Young's modulus of bi-layer material: experiments and numerical simulation, Surf. Coat. Technol. 200 (2005) 890–893.

[19] T. Ohmura, S. Matsuoka, K. Tanaka, T. Yoshida, Nanoindentation load-displacement behaviour of pure face centered cubic metal thin films on a hard substrate, Thin Solid Films 385 (2001) 198–204.

[20] Z.H. Xu, D. Rowcliffe, Finite element analysis of substrate effects on indentation behaviour of thin films, Thin Solid Films 447-448 (2004) 399–405.

[21] W.C. Oliver, G.M. Pharr, An improved technique for determining hardness and elastic modulus using load and displacement sensing indentation experiments, J. Mater. Res. 7 (1992) 1564–1583.

[22] S. Kim, P.N. Kumta, Sol–gel synthesis and characterization of nanostructured hydroxyapatite powder, Mater. Sci. Eng. B 111 (2004) 232–236.

[23] A. Balamurugan, S. Kannan, S. Rajeswari, Evaluation of TiO_2 coatings obtained using the sol–gel technique on surgical grade type 316 L stainless steel in simulated body fluid, Mater. Lett. 59 (2005) 3138–3143.

[24] J.E. Field, R.H. Telling, The Young Modulus and Poisson Ratio of Diamond, Research Note, Cavendish Laboratory, Cambridge, 1999.

[25] L. Hemmouche, D. Chicot, A. Amrouche, A. Iost, M.A. Belouchrani, X. Decoopman, G. Louis, E.S. Puchi-Cabrera, An analysis of the elastic properties of a porous aluminium oxide film by means of indentation techniques, Mater. Sci. Eng. A 585 (2013) 155–164.

[26] H. Gao, C.H. Chiu, J. Lee, Elastic contact versus indentation modeling of multi-layered materials, Int. J. Solids Struct. 29 (1992) 2471–2492.

[27] T. Kokubo, H. Takadama, How useful is SBF in predicting in vivo bone bioactivity? Biomaterials 27 (2006) 2907–2915.

[28] D.M. Liu, T. Troczynski, W.J. Tseng, Aging effect on the phase evolution of water-based sol–gel hydroxyapatite, Biomaterials 23 (2002) 1227–1236.

[29] K.A. Gross, C.S. Chai, G.S.K. Kannangara, B. Ben-Nissan, Thin hydroxyapatite coatings via sol–gel synthesis, J. Mater. Sci. Mater. Med. 9 (1998) 839–843.

[30] D.M. Liu, Q. Yang, T. Troczynski, Sol–gel hydroxyapatite coatings on stainless steel substrates, Biomaterials 23 (2002) 691–698.

[31] Z.H. Cheng, A. Yasukawa, K. Kandori, T. Ishikawa, FTIR study on incorporation of CO_2 into calcium hydroxyapatite, J. Chem. Soc. Faraday Trans. 94 (1998) 1501–1505.

[32] A.H. Rajabi-Zamani, A. Behnamghader, A. Kazemzadeh, Synthesis of nanocrystalline carbonated hydroxyapatite powder via nonalkoxide sol–gel method, Mater. Sci. Eng. C 28 (2008) 1326–1329.

[33] D.W. Holcomb, R.A. Young, Thermal decomposition of human tooth enamel, Calcif. Tissue Int. 31 (1980) 189–201.

[34] J.C. Elliott, The crystallographic structure of dental enamel and related apatitesPhD. Thesis University of London, 1974.

[35] O.C. Wilson Jr., R.E. Riman, Morphology control of lead carboxylate powders via anionic substitutional effects, J. Colloid Interface Sci. 167 (1994) 358–370.

[36] S. Yala, H. Khireddine, D. Sidane, S. Ziani, F. Bir, Surface modification of natural and synthetic hydroxyapatites powders by grafting polypyrrole, J. Mater. Sci. 48 (2013) 7215–7223.

[37] W. Feng, L. Mu-sen, L. Yu-peng, Q. Yong-xin, A simple sol–gel technique for preparing hydroxyapatite nanopowders, Mater. Lett. 59 (2005) 916–919.

[38] M. Aizawa, H. Ueno, K. Itatani, I. Okada, Syntheses of calcium-deficient apatite fibres by a homogeneous precipitation method and their characterizations, J. Eur. Ceram. Soc. 26 (2006) 501–507.

[39] Y.C. Tsui, C. Doyle, T.W. Clyne, Plasma sprayed hydroxyapatite coatings on titanium substrates part 1: mechanical properties and residual stress levels, Biomaterials 19 (1998) 2015–2029.

[40] T.J. Webster, C. Ergun, R.H. Doremus, R.W. Siegel, R. Bizios, Enhanced functions of osteoblasts on nanophase ceramics, Biomaterials 21 (2000) 1803–1810.

[41] D. Chicot, J. Mendoza, A. Zaoui, G. Louis, V. Lepingle, F. Roudet, J. Lesage, Mechanical properties of magnetite (Fe_3O_4), hematite (α-Fe_2O_3) and goethite (α-FeO·OH) by instrumented indentation and molecular dynamics analysis, Mater. Chem. Phys. 129 (2011) 862–870.

[42] B. Jönsson, S. Hogmark, Hardness measurements of thin films, Thin Solid Films 114 (1984) 257–269.

[43] T. Fu, C.S. Wen, J. Lu, Y.M. Zhou, S.G. Ma, B.H. Dong, B.G. Liu, Sol–gel derived TiO_2 coating on plasma nitrided 316 L stainless steel, Vacuum 86 (2012) 1402–1407.

[44] O. Borrero-López, M. Hoffman, A. Bendavid, P.J. Martin, Mechanical properties and scratch resistance of filtered-arc-deposited titanium oxide thin films on glass, Thin Solid Films 519 (2011) 7925–7931.

[45] T. Modes, B. Scheffel, C. Metzner, O. Zywitzki, E. Reinhold, Structure and properties of titanium oxide layers deposited by reactive plasma activated electron beam evaporation, Surf. Coat. Technol. 200 (2005) 306–309.

[46] B. Viswanath, R. Raghavan, U. Ramamurty, N. Ravishankar, Mechanical properties and anisotropy in hydroxyapatite single crystals, Scr. Mater. 57 (2007) 361–364.

[47] S. Saber-Samandari, K.A. Gross, Micromechanical properties of single crystal hydroxyapatite by nanoindentation, Acta Biomater. 5 (2009) 2206–2212.

[48] S. Saber-Samandari, K.A. Gross, Nanoindentation on the surface of thermally sprayed coatings, Surf. Coat. Technol. 203 (2009) 3516–3520.

[49] K.A. Gross, L.M. Rodriguez-Lorenzo, Sintered hydroxyfluorapatites. Part II: mechanical properties of solid solutions determined by microindentation, Biomaterials 25 (2004) 1385–1394.

[50] K.L. Ou, R.J. Chung, F.Y. Tsai, P.Y. Liang, S.W. Huang, S.Y. Chang, Effect of collagen on the mechanical properties of hydroxyapatite coatings, J. Mech. Behav. Biomed. Mater. 4 (2011) 618–624.

[51] K.A. Gross, S. Saber-Samandari, Revealing mechanical properties of a suspension plasma sprayed coating with nanoindentation, Surf. Coat. Technol. 203 (2009) 2995–2999.

[52] U. Vijayalakshmi, K. Prabakaran, S. Rajeswari, Preparation and characterization of sol–gel hydroxyapatite and its electrochemical evaluation for biomedical applications, J. Biomed. Mater. Res. A 87 (2008) 739–749.

[53] A.O. Olofinjana, J.M. Bell, A.K. Jamting, Evaluation of the mechanical properties of sol–gel-deposited titania films using ultra-micro-indentation method, Wear 241 (2000) 174–179.

[54] J. Song, Y. Liu, Y. Zhang, L. Jiao, Mechanical properties of hydroxyapatite ceramics sintered from powders with different morphologies, Mater. Sci. Eng. A 528 (2011) 5421–5427.

[55] J.Y. Rho, Y.T. Tsui, G.M. Pharr, Elastic properties of human cortical and trabecular lamellar bone measured by nanoindentation, Biomaterials 18 (1997) 1325–1330.

[56] K.H. Im, S.B. Lee, K.M. Kim, Y.K. Lee, Improvement of bonding strength to titanium surface by sol–gel derived hybrid coating of hydroxyapatite and titania by sol–gel process, Surf. Coat. Technol. 202 (2007) 1135–1138.